Int. J. Heat Mass Transfer. Vol. 36, No. 6, pp. 1677–1686, 1993
Printed in Great Britain

0017–9310/93 $6.00 + 0.00

Flow dynamics and heat transfer of a condensate film on a vertical wall—I. Numerical analysis and flow dynamics

ERICH STUHLTRÄGER
BALZERS Ltd, FL-9496 Balzers, Liechtenstein

YUTAKA NARIDOMI
Mitsubishi Heavy Industries Ltd, 2-1-1, Shinhama, Arai-machi, Takasago-shi 676, Japan

and

AKIO MIYARA and HARUO UEHARA
Saga University, 1, Honjo-machi Saga-shi, Saga 840, Japan

(*Received* 14 *November* 1991 *and in final form* 25 *February* 1992)

Abstract—The flow dynamics and heat transfer characteristics of the condensate film on a vertical wall is analysed by solving the time-dependent Navier-Stokes and the energy equation as well as the Poisson equation for the pressure with finite difference schemes and non-periodic boundary conditions. The simulation shows the evolution of the condensate film from the leading edge until 0.6 m by the low frequency surface fluctuation upstream of the line of wave-inception. Downwards, the time-averaged film thickness is decreasing with the flowing of big short waves, which are merging afterwards into individual long waves. The strong influence of the wave on the flow is shown by the pressure and vorticity field.

1. INTRODUCTION

THIN FILM condensation heat transfer is widely used in power plant systems, refrigeration equipment and many other industrial process equipment. The condensate film flow is divided into three regions such as laminar, wavy and turbulent regions. The heat transfer coefficient in the wavy and turbulent regions is much higher than in the laminar region, forcing the falling film as early as possible into the state of big roll wave lumps gliding on a thin substrate layer. This is one of the most efficient means of increasing the heat flux. Contrary to existing opinion that there exists a waveless region immediately after the initiation of the condensate film, Marschall and Lee [1] showed by the stability analysis that the distance from the leading edge of the condensation film until the location where the film is unstable is negligibly small for practical situations. The understanding of the development of the condensate flow from the leading edge, the very beginning of the falling film, down to the wavy state is therefore, important and since it has not been covered by publications until now, lead to the investigations presented herewith.

Flow visualization studies of Dukler and Bergelin [2] reveal a thin laminar condensate film growing from the top of the plate. By flowing downward, small ripple waves can be seen on the instable surface at Reynolds numbers $Re > 20$, which are growing to distorted sinusoidal waves. The straight crests gradually bend and get higher to form intermediate waves at $Re > 100$. These waves steepen on their front at $Re > 1500$ and merge into lumps of roll waves, gliding on the thin film substrate, which may also be turbulent [3].

The heat flux through the film at constant wall and vapor temperature is on the one hand determined by the film thickness of the substrate, and on the other hand by the flow state, either laminar, wavy or turbulent with roll waves. The theoretical calculations of the laminar flow part at the beginning of the gravity driven condensate film [4] and the calculations including the effects of subcooling and the variation of the physical properties with temperature [5] have also been confirmed by the experiments of Grigull [6]. As for the wavy and turbulent falling film without condensation, not only the time averaged film thickness and Reynolds number but also the statistics of the wave frequencies as well as wave amplitudes, length and celerity were determined in comprehensive experimental studies [7–13], covering the range up to $Re = 13\,000$.

In order to calculate the flow and heat flux of the falling film in the wavy state, many different theories have been established. The results fit the experimental data to a certain extent, since the calculation schemes are restricted by periodicity, space and time averaging and linearization. Penev *et al.* [14] used an integral method to solve the Navier–Stokes equation and linearized it for the approximation of small wave amplitudes. The wave numbers, wavelengths and phase-velocity can be predicted for small Weber numbers.

NOMENCLATURE

A variable, stands for u, v or p [—]
B variable, stands for u, v or p [—]
c celerity, c^*/u_0 [—]
c_p specific heat of liquid at constant pressure [J kg^{-1} K^{-1}]
f^+ distortion factor
f frequency [Hz]
Fr Froude number, $u_0^2/(g\delta_0)$ [—]
G mass flow rate of film per unit film width, [kg m^{-1} s^{-1}]
h heat transfer coefficient [W m^{-2} K^{-1}]
H dimensionless parameter, $c_p(T_s - T_w)/L$ [—]
i mesh point index number in x-direction [—]
I biggest mesh point index number in x-direction at the outflow [—]
j mesh point index number in y-direction [—]
J biggest mesh point index number in y-direction, beyond surface [—]
J_s index number of the surface point [—]
k thermal conductivity of liquid [W m^{-1} K^{-1}]
L latent heat [J]
Nu Nusselt number, hx/k [—]
p pressure
Pr Prandtl number [—]
Re film Reynolds number, $4G/\mu$ [—]
Re_0 film Reynolds number at the outflow location, $u_0\delta_0/\nu$ [—]
t time
T temperature
u velocity parallel to the condensation plate [—]
v velocity perpendicular to the condensation plate [—]
We Weber number, $\rho_0 u_0^2 \delta_0/\sigma$ [—]
x coordinate parallel to the condensation plate [—]
y coordinate perpendicular to the condensation plate [—].

Greek symbols
Γ dimensionless surface tension, $\sigma(\nu^4 g)^{-1/3}/\rho$ [—]
δ film thickness [—]
ζ relaxation factor in SOR-method [—]
η transformed y-coordinate in the calculation plane [—]
λ wavelength [—]
μ dynamic viscosity [kg s m^{-1}]
ν kinetic viscosity [m^2 s^{-1}]
ξ variable, stands for x, η [—]
ρ density of liquid [kg m^{-3}]
σ surface tension [N m^{-1}]
Ω vorticity [—].

Subscripts
l liquid
0 standard value at the outflow location
s surface
v vapor
w wall
x local value at the position x.

Superscripts
* parameter having its dimension
- time averaged value.

Hirshburg and Florschuetz [15, 16] established the linearized theory in a coordinate system moving with the wave by assuming periodicity and a parabolic profile. The sinusoidal and the intermediate wave state were got as asymptotic solutions, in which the intermediate wave named Kapitza [8] has long teardrop shapes with relatively steep wavefronts similar to single waves. They introduced a parameter f^+, which is the ratio of the actual frequency to the most unstable frequency of the wave and indicates the distortion of the wave from the sinusoidal wave. f^+ varies from the sinusoidal wave $f^+ = 1$ to the intermediate wave $f^+ = 0.35$. The calculated wave-frequencies, amplitudes, celerities and lengths agree well with the experimental values for $Re < 400$. The calculated space and time averaged Nusselt number predicts well the experimental results. Rao and Sarma [17] developed a laminar two film layer model for the momentum and energy equations, which are integrated over the film thickness. The influence of parameters, like the Prandtl number and the gravitational force, on the local film thickness and the Nusselt number are shown and compared with the Nusselt solution. Brauner [18] establishes a four region and a periodic model for the roll wave on the thin substrate layer, and calculates the film thickness and wave-celerity and frequency for the laminar and turbulent case. The results agree well in the region $1000 < Re < 10\,000$ with the experimental ones.

Because the evolution of the film in time and space as well as the local heat transfer coefficient can be neither calculated by analytical theories nor accurately measured, attempts have been made recently to solve the unsteady basic equation by either finite element or finite difference methods. The two-dimensional computer calculations published up to now are focused mainly on one wave, which is in reality a highly three-dimensional phenomenon. Moreover the

equations were solved by using periodic boundary conditions. Bach and Villadsen [19] solved the two-dimensional Navier–Stokes equation for a highly three-dimensional roll wave with finite element method in a coordinate system which moves with the wave. The stationary solution is calculated for given physical parameters and wave shape factors by taking a wave with a form close to the stationary one as initial condition. When the shape does not change any more, the solution is assumed to be attained. The final wave structure, the stationary velocities and pressure are obtained and agree with the limited experimental data. Also Wasden and Dukler [20] investigated the roll wave two-dimensionally. They solved the basic equations with the available finite difference codes TEACH-T and SIMPLER for a roll wave with different experimentally determined surface shapes. They got the streamline maps and wall shear-stress, but do not show the pressure distribution. Again, Moalem *et al.* [21] calculated the roll wave by solving the three-dimensional basic equations with the available finite difference code FLOW3D and finite element code FIDAP in a coordinate system moving with the wave. They started from a prescribed wave form and calculated the evolution of one wave gliding on a substrate with a given thickness in front and in the back of the wave. The wave shape and the streamlines in the wave are obtained.

The computer capacities at the moment do not allow to calculate the whole film flow and the local heat flux three-dimensionally from the beginning of the condensate film until the region of roll waves, as the results of Marschall and Lee [1] suggests.

In these investigations, the condensate film flow without interfacial shear is calculated in the first part, the region from the leading edge of the film until the occurrence of distorted sinusoidal waves. The vapor is assumed to be saturated. The flow field and heat flux are calculated by two-dimensional direct computer simulation with non-periodic boundary conditions and without turbulence model. Since the flow in this region is still mainly two-dimensional, the two-dimensional calculation is not a major restriction. The calculations are overcoming the restrictions, like periodicity, fixed boundary conditions or previous experimentally determined wave shapes.

2. NUMERICAL SIMULATION METHOD

The computer simulation was performed for an incompressible viscous liquid in the field of the condensate film flow. R11 was chosen as the medium for three reasons at the condition of the Prandtl number $Pr = 4.3$ and the ratio $H = c_p(T_s - T_w)/L = 0.06$. First, the properties of R11 are well known. Second, the dimensionless surface tension is with $\Gamma = 2671$ so big that the line of inception is at a reasonable small distance downward of the starting point of condensation, allowing a relatively small calculation area to be used. Third, due to the fluid properties, the condensate film is growing relatively fast with increasing distance from the beginning of the film. By this, more accurate measurements can be made, which are needed for the validation of the computer calculation. The two-dimensional time-dependent Navier–Stokes equations, the Poisson equation for the pressure and the linearized energy equation were solved with a finite difference scheme. The basic equations were non-dimensionalized with the surface velocity u_0 and the film thickness δ_0 at the outflow location of the calculation field obtained from the Nusselt theory. The coordinate and velocity parallel and perpendicular to the wall are $x = x^*/\delta_0$, $y = y^*/\delta_0$, $u = u^*/u_0$ and $v = v^*/v_0$, respectively. The pressure is $p = p^*/(\rho_0 u_0^2)$ and the time $t = t^*/(\delta_0/u_0)$.

The equation of continuity and the Navier–Stokes equations are

$$\frac{\partial u}{\partial x} + \frac{\partial v}{\partial y} = 0 \tag{1}$$

$$\frac{\partial u}{\partial t} + u\frac{\partial u}{\partial x} + v\frac{\partial u}{\partial y} = -\frac{\partial p}{\partial x} + \frac{1}{Re_0}\left(\frac{\partial^2 u}{\partial x^2} + \frac{\partial^2 u}{\partial y^2}\right) + \frac{1}{Fr} \tag{2}$$

$$\frac{\partial v}{\partial t} + u\frac{\partial v}{\partial x} + v\frac{\partial v}{\partial y} = -\frac{\partial p}{\partial y} + \frac{1}{Re_0}\left(\frac{\partial^2 v}{\partial x^2} + \frac{\partial^2 v}{\partial y^2}\right) \tag{3}$$

where Re_0 is the film Reynolds number at the outflow position obtained from the Nusselt theory and Fr the Froude number. The Poisson equation is the divergence of the Navier–Stokes equations (2), (3)

$$\frac{\partial}{\partial t}\left(\frac{\partial u}{\partial x} + \frac{\partial v}{\partial y}\right) + \left(\frac{\partial u}{\partial x}\right)^2 + \left(\frac{\partial v}{\partial y}\right)^2 + 2\frac{\partial v}{\partial x}\frac{\partial u}{\partial y} + u\left(\frac{\partial^2 u}{\partial x^2} + \frac{\partial^2 v}{\partial x\,\partial y}\right) + v\left(\frac{\partial^2 v}{\partial y^2} + \frac{\partial^2 u}{\partial x\,\partial y}\right) = -\nabla^2 p + \frac{1}{Re_0}\left[\frac{\partial}{\partial x}(\nabla^2 u) + \frac{\partial}{\partial y}(\nabla^2 v)\right]. \tag{4}$$

Although the theoretical value of $(\partial u/\partial x + \partial v/\partial y)$ is zero, the first terms of the left hand side were retained in order to prevent accumulation of numerical errors. The fifth and sixth terms of the left hand side were simplified with the help of the equation of continuity. The second term on the right hand side was retained because of the low Reynolds number. The Poisson equation became therefore:

$$\nabla^2 p = -\frac{\partial D}{\partial t} - \left(\frac{\partial u}{\partial y}\right)^2 - \left(\frac{\partial v}{\partial y}\right)^2 - 2\frac{\partial v}{\partial x}\frac{\partial u}{\partial y} + \frac{1}{Re_0}\left(\frac{\partial^2 D}{\partial x^2} + \frac{\partial^2 D}{\partial y^2}\right) \tag{5}$$

$$\frac{\partial}{\partial t}\left(\frac{\partial u}{\partial x} + \frac{\partial v}{\partial y}\right) = \frac{\partial D}{\partial t}. \tag{6}$$

Only the linearized energy equation without inter-

facial shear stress was used. Koh *et al.* [22] reported that the interfacial shear shows no influence on the local Nusselt number for conditions calculated in this paper. Ueda and Tanaka [23] showed by temperature measurements a thick conduction layer adjacent to the wall and a thin uniform temperature layer near the liquid–vapor interface, so that a nearly linear temperature profile was assumed. The dimensionless temperature is $T = (T^* - T_w)/(T_s - T_w)$

$$\frac{\partial^2 T}{\partial y^2} = 0. \tag{7}$$

The increase of the film thickness by condensation of saturated vapor was calculated by using the linearized energy balance

$$\frac{k}{\delta}(T_s - T_w)\,\mathrm{d}x = \frac{L'\rho g \delta^2}{\mu}\,\mathrm{d}\delta \tag{8}$$

where the effect of non-linearity suggested by Rohsenow [24] was taken into account by setting

$$L' = L + 0.68 c_p (T_s - T_w). \tag{9}$$

The effect of the variation of the properties with temperature was approximated by the mean of Minkowycz and Sparrow [25]. k, ρ, ν and c_p were calculated at the temperature

$$T = T_w + 0.3(T_s - T_w). \tag{10}$$

The calculations were done in a regular mesh (x, η). The transition function to the irregular mesh in the physical (x, y)-plane (Fig. 1) is of polynomial form for the y-coordinate

$$y = 3.68 \times 10^2 \eta - 1.33 \times 10\eta^2 + 4.05 \times 10\eta^3. \tag{11}$$

The basic equations were rewritten for the calculation in the (x, η)-plane with the derivatives

$$\frac{\partial A}{\partial y} = \frac{\partial A}{\partial \eta}\left(\frac{\partial y}{\partial \eta}\right)^{-1} \tag{12}$$

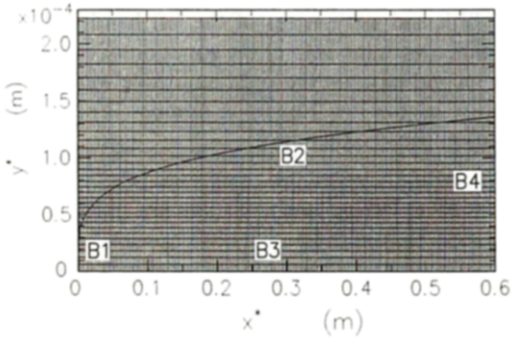

FIG. 1. Calculation region, boundaries and irregular staggered grid of the wall parallel velocity u; every fourth line in x-direction and every second one in y-direction of the (770×32) grid is drawn: velocity perpendicular to the wall v, pressure p and vorticity Ω.

$$\frac{\partial^2 A}{\partial y^2} = \frac{\partial}{\partial y}\left[\frac{\partial A}{\partial \eta}\left(\frac{\partial y}{\partial \eta}\right)^{-1}\right]$$

$$= \frac{\partial^2 A}{\partial \eta^2}\left(\frac{\partial y}{\partial \eta^2}\right)^{-2} - \frac{\partial A}{\partial \eta}\frac{\partial^2 y}{\partial \eta^2}\left(\frac{\partial y}{\partial \eta}\right)^{-3} \tag{13}$$

where A stands for u, v, p.

The Poisson equation was solved with the Successive Over-Relaxation Method (SOR). Since the boundary conditions are complicated, an analytical calculation for the relaxation factor cannot be done. The relaxation factor was first calculated for Neumann boundary conditions and by varying the factor in the real field slightly, the one with the fastest convergence turned out to be $\xi = 1.66$. The SOR iteration was stopped, when the pressure difference between two iteration steps was smaller than 10^{-8}.

The timestep advance was made with the Euler explicit scheme

$$\frac{\Delta A}{\Delta t} = \text{r.h.s.-terms of } N\text{–}S \text{ equation.} \tag{14}$$

The third order upwind scheme, proposed by Kawamura and Kuwahara [26] was used for the convective term in the Navier–Stokes equations

$$\left(A\frac{\partial B}{\partial \xi}\right)_{i,j} = A_{i,j}[-B_{i+2,j} + 8(B_{i+1,j} - B_{i-1,j})$$

$$+ B_{i-2,j}]/(12h) + |A_{i,j}|(B_{i+2,j} - 4B_{i+1,j} + 6B_{i,j}$$

$$- 4B_{i-1,j} + B_{i-2,j})/(4h) \tag{15}$$

where A and B stands for the velocities u or v and for the coordinate x or η. This scheme introduces a numerical viscosity, which is proportional to the fourth order derivative of the velocity and dissipates the high wave number motion. Employing the third order upwind scheme of equation (15), Miyauchi and Tani [27] showed with three dimensional simulations of homogeneous isotropic turbulence that the energy spectra and the kinetic energy are in good agreement with the experiment of Comte-Bellot and Corrsin [28]. The scheme was used by Kawamura and Kuwahara [26] not only for the simulation of large scale structures, like the evolution of the wake behind a cylinder, but also for the transition from laminar to turbulent pipe flow. Stuhlträger *et al.* [29] used this scheme for the calculation of the coherent structures in the excited round jet and got good agreement with the experiment. Since no model is used for the turbulent viscosity, this scheme is well adapted to simulate the transition from laminar to turbulent flow. The central difference scheme was employed for all the other terms.

The calculations were carried out in a rectangular region on the staggered grid points (Fig. 1). In order to see the influence of the outflow boundary conditions, the region had been varied. Since the mesh size is crucial for capturing the wavelength and amplitude of the unstable waves, the mesh and also the

mesh size had been varied. The different grids have $I = 193$, 385 and 770 points in the region $0 < x < 4500$ as well as $0 < x < 2000$ and $J = 32$ and 64 in the region $0 < y < 1.5$. The smallest mesh in the y-direction has been adapted to be on the surface at the line of inception and with $y = 0.03$ so small that it can resolve 1/4 of the smallest measured amplitude [20] of the most unstable wave. The biggest mesh at the outermost position of a wave peak is $y = 0.05$. The size of the smallest mesh in axial direction has been chosen to cover well the most unstable wavelength by 8 points. Given the minimal mesh size in y-direction, the Courant-number at which stable calculations were obtained is 0.124.

3. BOUNDARY AND INITIAL CONDITIONS

Among the primitive variables, only velocities and the wave propagation values have been measured and can therefore be used for comparsion with the simulated results. From this consideration, only as few as necessary well defined velocity boundary conditions were used in this calculation. All other values for the boundary condition of the velocity and pressure were enabled to develop freely. This idea was supported by the results of testing of many combinations of velocity and pressure boundary conditions in the excited round jet [29]. In the case that the velocity and pressure are given at the same boundary by fixed values, distortion and oscillations occur, since they are depending on each other and cannot be given exactly at the same time by the finite difference scheme.

In these calculations, the boundary conditions were chosen in the way that only the velocity and the film thickness of the Nusselt theory had to be set on boundary B1 (Fig. 1) for the first three rows, which are required by the third order upwind scheme. The grid for the velocity u was placed on the wall surface B3 and the one of v was put before and behind the surface. A_0 and $\partial^2 A_0/\partial\xi^2$ were set equal to zero, which gives the following nodal row values:

$$u(i,0) = 0 \tag{16}$$

$$u(i,-1) = -u(i,1) \tag{17}$$

$$v(i,0) = -v(i,1). \tag{18}$$

Since the third order upwind scheme for the convective terms on the Navier–Stokes equations require in every direction two adjoining points to the center point, the donor cell method of Gentry *et al.* [30], which needs only one adjoining point, was employed on the nodal points $A(i, J-1)$ on the surface boundary B2 and on the column points $A(I-1, j)$ on the outflow boundary B4. Here, the donor cell method is given only for the boundary B2:

$$\left(A\frac{\partial B}{\partial x}\right)_{i,j} = \frac{A_{R,j}B_{R,j} - A_{L,j}B_{L,j}}{\Delta x} \tag{19}$$

with

$$A_{R,j} = \tfrac{1}{2}(A_{i+1,j} + A_{i,j}) \tag{20}$$

$$A_{L,j} = \tfrac{1}{2}(A_{i,j} + A_{i-1,j}) \tag{21}$$

$$B_{R,j} = B_{i,j}(A_{R,j} > 0)$$

$$B_{R,j} = B_{i+1,j}(A_{R,j} < 0) \tag{22}$$

$$B_{L,j} = B_{i-1,j}(A_{L,j} > 0)$$

$$B_{L,j} = B_{i,j}(A_{L,j} < 0). \tag{23}$$

The boundary condition at the outflow B4 determines sensitively the distortion of the outflow region and its upstream influence so that it is not enough to have stable outflow boundary conditions. Simple and straight-forward boundary conditions, like constant vorticity, need only few calculation steps, but the influence on the upstream field is big, where as complicated conditions give a smooth outflow, but require many calculation steps. Among different tested boundary conditions [29], the method of Shapiro and O'Brien [31] was chosen and also used for these calculations. Linear extrapolation is used in this method, in order to follow the Lagrange trajectory of a particle and to get outflow boundary value. The case of $v > 0$ is shown in Fig. 2

$$A' = A_{I,j} + \frac{\bar{u}\Delta t}{\Delta x}(A_{I-1,j} - A_{I,j}) \tag{24}$$

$$A'' = A_{I,j-1} + \frac{\bar{u}\Delta t}{\Delta x}(A_{I-1,j-1} - A_{I,j-1}) \tag{25}$$

$$A = A' + \frac{\bar{v}\Delta t}{\Delta \eta}(A'' - A'). \tag{26}$$

The velocity $u(i, J)$ nearest to the surface B2 was interpolated by a parabolic curve determined from the velocity on the surface velocity $u_s(i)$ and the two velocities $u(i, J-1)$ and $u(i, J-2)$. The surface velocity u_s was calculated from the Navier–Stokes equation. The velocity $v(i, J)$ was got from the equation

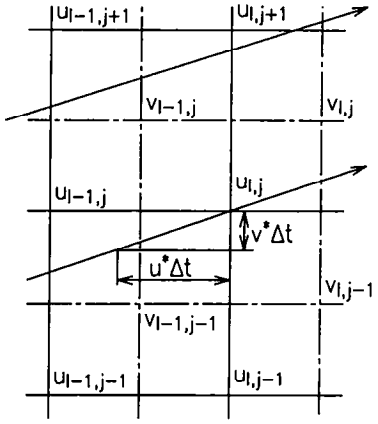

FIG. 2. Outflow boundary condition of Shapiro and O'Brien [31] in the staggered grid, shown for the wall parallel velocity u.

of continuity and the one on the surface $v_s(i)$ by setting the derivative $\partial v/\partial \eta = 0$.

Because of the staggered grid, only the pressure of the outermost points cannot be calculated by SOR. Therefore, the pressure at the outermost boundary points $p(i, 1)$ on B3 were got by calculating first the pressure derivative $\partial p/\partial \eta$ between $p(i, 2)$ and $p(i, 1)$ with the Navier–Stokes equation. Then, the pressure $p(i, 1)$ was linearly extrapolated from the pressure $p(i, 2)$ with the calculated pressure derivative. The pressure at the outflow boundary points $p(I, j)$ cannot be calculated in the same way as the points $p(i, J)$, since the velocity was already calculated by the Navier–Stokes equation by using the second order scheme. The outermost points were obtained with the backward difference formula by using the points $p(I-3, j)$, $p(I-2, j)$ and $p(I-1, j)$

$$p_{I,j} = p_{I-1,j} + (3p_{I-1,j} - 4p_{I-2,j} + p_{I-3,j})/2. \quad (27)$$

The surface is assumed to be a free surface with no shear-stress. With the assumption that the wavelength is much bigger than the film thickness, the surface pressure $p_s(i)$ was calculated by

$$(p - p_s) + \frac{1}{We}\frac{\partial^2 \delta}{\partial x^2} + \frac{8}{Re_0}\frac{\partial u_s}{\partial x} = 0. \quad (28)$$

The pressure $p(i, J)$ was linearly interpolated from the surface pressure $p_s(i)$ and $p(i, J-1)$.

The displacement of the surface was calculated after every time step from the surface velocity by using $\Delta x_s = u_s \Delta t$, $\Delta y_s = v_s \Delta t$ and from the increase of the film thickness due to the condensation by using the energy balance equation (8).

As for the initial condition, the film thickness δ_0 and the velocity u_s of the Nusselt solution [4] including the parabolic profile inside the film was used. The velocity $v(i, j)$ was set to be zero. The pressure $p(i, j)$ is the same as the surface pressure $p_s(i)$, calculated from equation (28).

Starting from the initial conditions, the calculations were first done until the steady state. Steady state is reached, when on the one hand the time-averaged velocities and film thickness as well as the root mean square (r.m.s.) velocities are not changing any more. On the other hand, when the simulation time is bigger than the travelling time of a particle on the surface from the beginning to the outflow point. The results were then taken from calculation sets of a real time of one second.

4. RESULTS

The analysis of the wave shapes and the film fluid dynamics are shown in part I of this paper. The connection of the fluid dynamic aspects to the increase of the heat transfer coefficient are presented in part II.

The thickness of the film in the whole field, taken at every 1/16 s in real time, reveals the evolution of the surface instability at the line of inception into sinusoidal waves, which are merging downstream into harmonic waves (Fig. 3) and by this, doubling the experimental findings [2]. The line of inception is not at a fixed location, but fluctuates up and down stream. After the first strong growth downward of the line of inception, the amplitude of the wave is increasing only slightly. This figure reveals also that the wave amplitude and length at the same x-location are not constant but are fluctuating. The progression of the wave can well be seen by the rows they are forming in the multi-graph (Fig. 3). Gradual increasing of the inclination angle of these rows of waves from the line of inception until the merging into long waves downstream indicates the increase of the wave celerity.

Since the measurement and even the visual inspection [3] of the laminar film with ripple waves as surface instability is very difficult, the unsteady computer simulation gives new insights. Because the fluctuations are very small, the time averaged film thickness is subtracted from the instantaneous ones and the change of the film thickness at successive time intervals shown again after magnification (Fig. 4). The surface in the laminar region is slightly moving upward and downward in a low frequency fluctuation. This fluctuation goes together with the fluctuation of

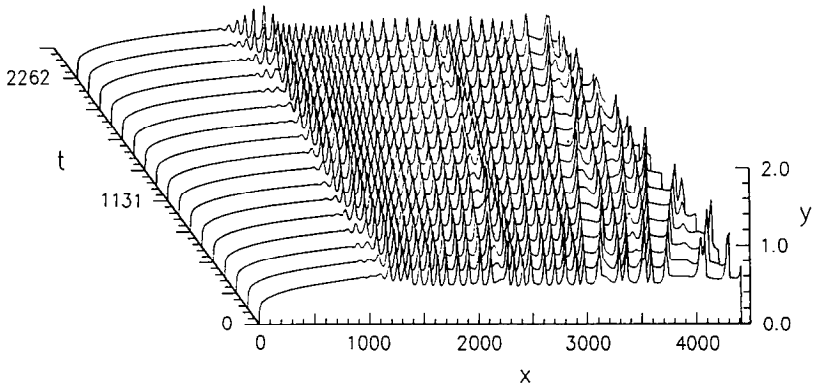

FIG. 3. Instantaneous surface location of the film in the whole calculation region at every 1/16 s after the steady state.

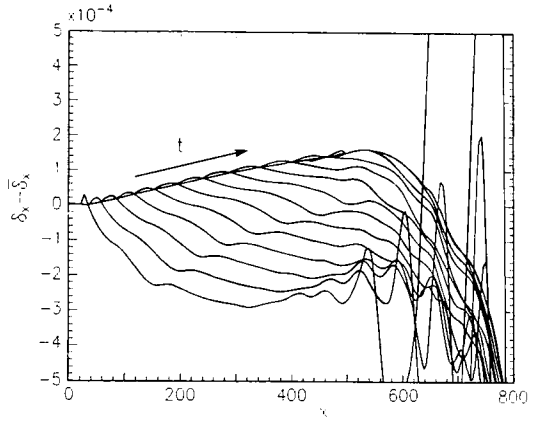

FIG. 4. Instantaneous surface location of the film in the region from the leading edge until the strong growth of the waves at the line of inception at every 1/16 s after the steady state.

the location of the line of inception and with the upstream feedback of the rapid growth of the sinusoidal waves. Supporting the stability analysis of Marschall and Lee [1], surface instability occurs at early stage and moves on the surface downward and may induce the early and rapid growth of the sinusoidal waves at the line of inception. The time-step advance of the simulation allows to observe the motion and the evolution of the ripple waves. Its celerity and wave length can well be determined (Figs. 6, 7). The wave celerity of the ripple waves is smaller than the measured one of the falling film without condensation [7–10], showing the influence of the condensation by which the waves are slowed down.

The time averaged film thicknesses of the computer simulation, the experiments [9, 32–35] and the Nusselt theory increase in the laminar region until the line of inception (Fig. 5). The film thickness of the Nusselt theory is slightly bigger than the experimental and computer simulated one. Considering the bigger difference of the average film thickness between the Nusselt theory and the experiment as well as the computer simulation when big surface waves are present, the small difference in the laminar region can be explained by the influence of the ripple waves and the low frequency surface fluctuation. The film thickness is decreasing during the rapid growth of the sinusoidal waves at $70 < Re_x < 140$, which goes together with

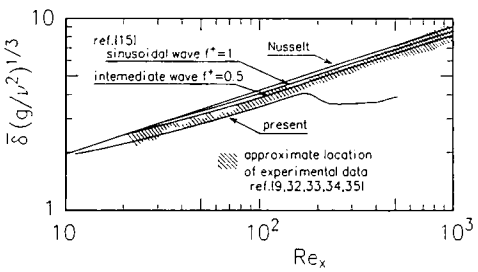

FIG. 5. Time-averaged film thickness of the present simulation, the Nusselt theory and the experiments [9, 32–35].

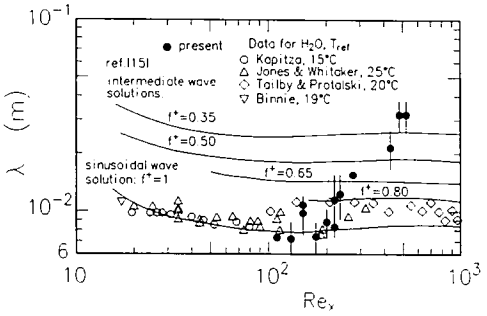

FIG. 6. Wave-length of the present simulation of the condensation film, the theory of Hirshburg and Florschuetz [15] and experiments [7, 8, 10, 36] for the falling film without condensation.

the strong increase of the wave celerity. Further downstream at $Re_x > 220$, when the wave amplitude is increasing only slightly, the film thickness increases again. In this region, the computer simulated film thickness is much smaller than the one of the Nusselt theory, which does not take the surface waves into account.

The computer simulated wave-lengths are taken from a big number of waves at every location (Fig. 6). The fluctuations, therefore, are shown with bars. Although the simulated results are in good agreement with the experiments of the falling film of water at $110 < Re_x < 220$, they increase quickly from $Re_x = 220$ where the waves begin to merge. Hirshburg and Florschuetz [15] calculated the wavelength of different wave forms (sinusoidal to intermediate wave state) for the case of the falling film without condensation. By comparing these wave shapes and wave lengths with the ones of the computer simulation, the same order of wavelength can be observed for $Re > 110$. Hirshburg and Florschuetz [15] considered a falling film without condensation and used as upstream boundary condition at $Re < 100$ a film of a given thickness, which allows the long wave instability to grow into short sinusoidal waves. The condensate film, however, whose thickness increases from a very thin film in the laminar region, has short wave instability. This short-wave instability is growing at

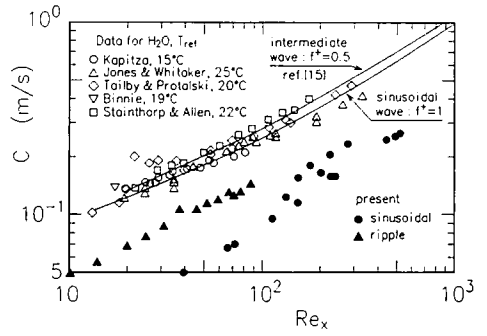

FIG. 7. Wave-celerity of the simulation of the condensation film and comparison with the experiments [7–10, 36] for the falling film without condensation.

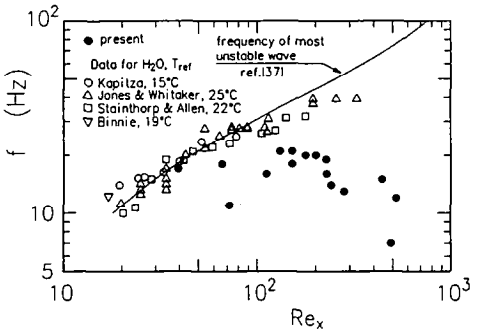

FIG. 8. Wave-frequency of the present simulation, the experiments [7–10] and also the theory [37] for the falling film without condensation.

$110 < Re < 220$ into sinusoidal waves with about the same wave-length as the one of the falling film.

The celerity of the ripple waves on the condensate film is increasing with the same rate but it is smaller than the celerity of the waves of the falling film without condensation due to the effect of the condensation (Fig. 7). The sinusoidal waves, however, which are growing into big waves, have a smaller celerity than the ripple waves at the beginning of their detection. It could not be sorted out during the detection of the sinusoidal waves, whether they are growing from low frequency fluctuations or from ripple waves, which are slowed down during the strong increase of their amplitude. During the strong growing at $70 < Re_x < 140$, the celerity is increasing quickly and is reaching about the same celerity level and increase as the ripple waves.

The frequency of the surface wave was obtained from the Fast Fourier Transformation of the film thickness, which was stored at every time step and at every eighth mesh point during the calculation (Fig. 8). The frequency of the ripple and sinusoidal wave at low Reynolds number increases slightly in the region of about 19 Hz and continues to decrease strongly after the big growth at the beginning of the merging of the waves at $Re_x > 200$. For a falling film without condensation, however, the theory of Pierson and Whitaker [37] predicts the most unstable frequency to increase with the Reynolds number. The reason for the different behavior due to condensation is again that the falling film has a given thickness

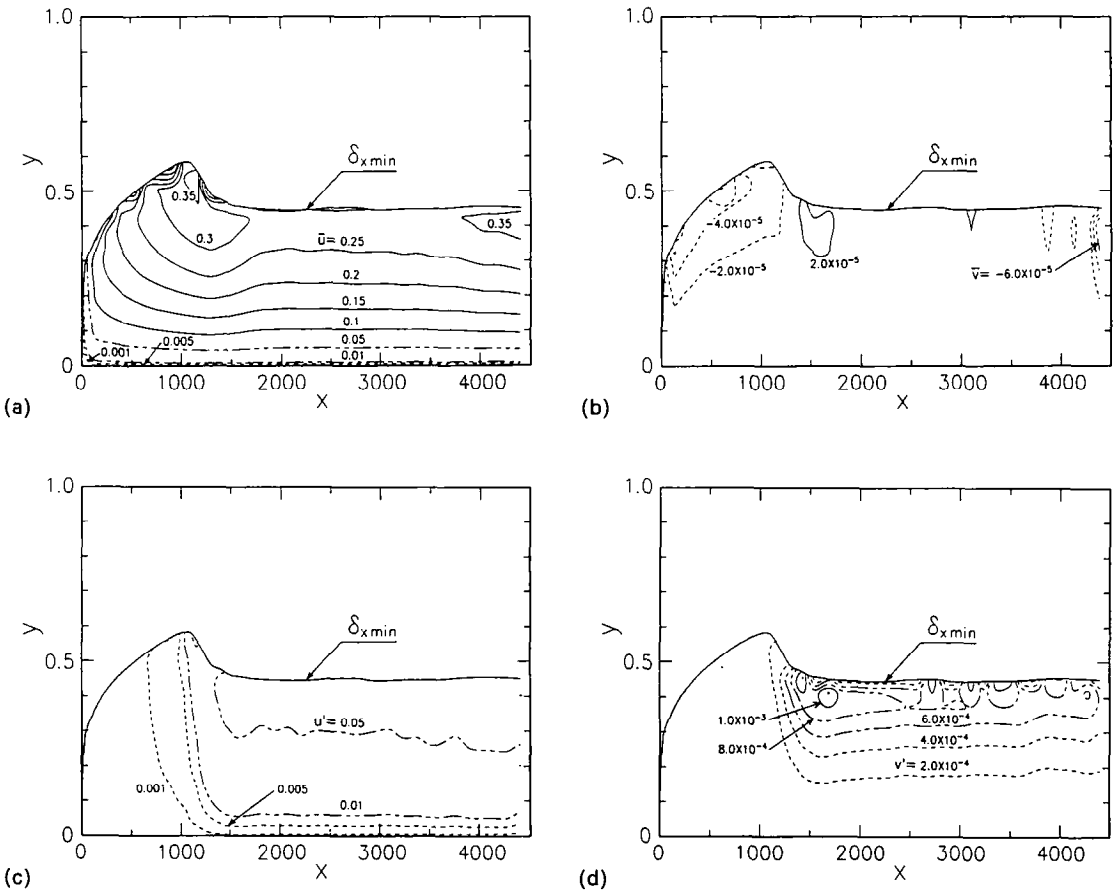

FIG. 9. Contours of the time-averaged and r.m.s. velocities; (a) $\bar{u}$, (b) $\bar{v}$, (c) u', (d) v'. Contour levels of u: 0.001, 0.005, 0.01, 0.05, 0.1, 0.15, 0.2, 0.3, 0.35; of v: -6.0×10^{-5}, -4.0×10^{-5}, -2.0×10^{-5}, 2.0×10^{-5}; of u': 0.001, 0.005, 0.01, 0.05 and of v': 2.0×10^{-4}, 4.0×10^{-4}, 6.0×10^{-4}, 8.0×10^{-4}, 1.0×10^{-3}.

at the beginning and the instability start with low frequency and long wave length. The theory [37] did not include a merging of waves at higher Reynolds number and could therefore not predict a decrease of the frequency. The most unstable wavelength at the line of inception does not differ much from the experimental results. Stainthorp and Batt [38], however, reported a decrease of the wave frequency of 50% from $Re_x > 100$ over a flow length of 0.6 m. The computer calculation predicts about the same decrease of the frequency on the same flow length. The experiments [9, 10] and the theory [37] show the most unstable frequency at $f = 25$ Hz at about $Re_x = 80$, the computer simulation gives the one at $f = 19$ Hz at $Re_x = 70$–140.

The time-averaged and r.m.s.-velocities can only be taken in the region which is always on the liquid side of the surface (Fig. 9). This region is bounded by the surface until the line of inception and by the deepest wave troughs farther downstream. Because of this, the maximum time-averaged velocity $\bar{u}$ is on the surface at the line of inception (Fig. 9(a)). The $\bar{u}$-velocity in the trough region is slightly smaller. The $\bar{v}$-velocity is negative in the region of the ripple waves near the surface due to condensation and increases to zero near the wall (Fig. 9(b)). In the trough region, which is mostly just beyond the surface, the $\bar{v}$-velocity is slightly negative and positive. The r.m.s.-velocity fluctuation u' and v' are very small in the region of the ripple waves and have their peaks in the region of the strong waves (Fig. 9(c), (d)). The fluctuations in the trough region are slightly smaller than the peak values and they decrease gradually in direction of the wall. This result is confirmed by the velocity and temperature measurements of Ueda and Tanaka [23] and supports the assumption that the heat flux perpendicular to the wall occurs mainly by conduction. The big fluctuation near the surface, however, indicate a mixing and would suggest a flattening of the temperature profile.

The influence of the outflow boundary condition [30] on the upstream field can well be seen from the time averaged and r.m.s.-values. Also in the fields of other size, the distortion of the time-averaged values is in the region of about $x = 3800$–4500 at the outflow. The r.m.s.-values do not show a remarkable distortion.

The instantaneous values of the velocity is shown by the velocity vector field (Fig. 10). In order to show the movement of the particles in the wave, the u-velocity is shifted by the wave celerity. The influence of the wavy flow on the particle movement in the substrate can be seen as deep down as $y = 0.1$ (Fig. 10(a)). The particles in the waves are accelerated and heaved in the front and let down in their back. It shows that although the wave amplitude is already big compared to the substrate thickness, the waves are still not roll waves. The big influence of the wave on the film up to the wall is also shown by the vorticity, whose vorticity peak at the wall beyond the

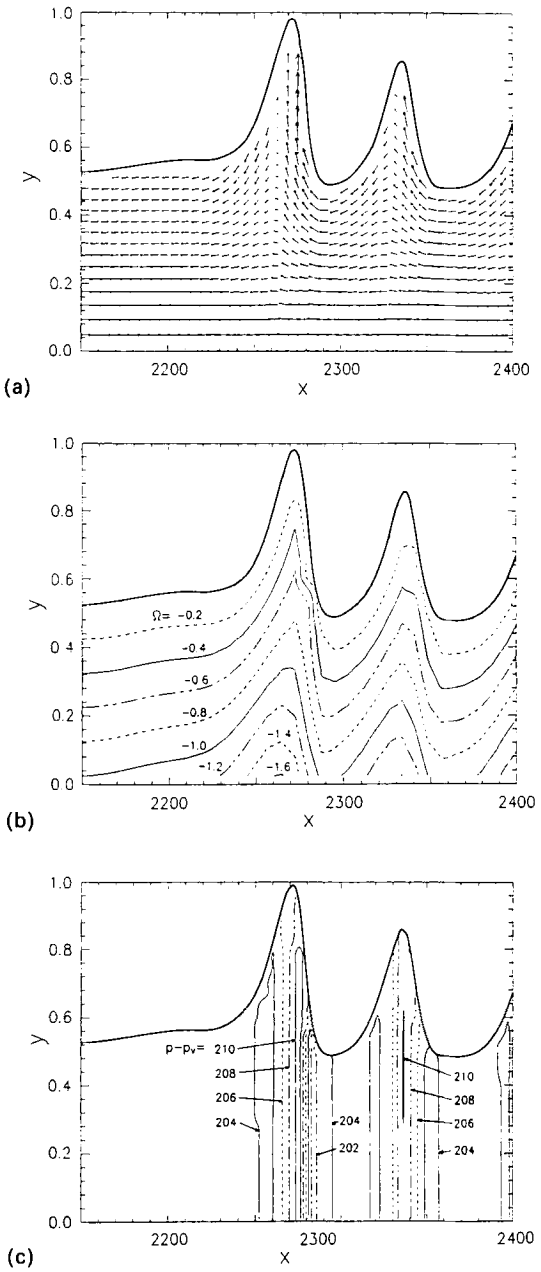

FIG. 10. (a) Velocity vectors, (b) vorticity Ω and (c) pressure $(p-p_v)$ of the instantaneous wave. Contour levels of Ω: -0.2, -0.4, -0.6, -0.8, -1.0, -1.2, -1.4, -1.6 and of $(p-p_v)$: 0.202, 0.204, 0.206, 0.208, 0.210.

wave crest is absolutely about 60% bigger than the wall vorticity beyond the ripple wave surface (Fig. 10(b)). The vorticity at the wall in the trough region is about the same as in the ripple wave region. The instantaneous pressure is biggest in the region beyond the wave crest and decreases to a minimum in the region beyond the trough (Fig. 10(c)). The pressure due to the surface tension dominates the pressure within the film so that there is little variation in x-direction, where one has to notice the scale of the figure with a ratio of wave length to wave peak thickness of $x/y \simeq 50$.

5. CONCLUSIONS

The direct computer simulation of the vertically falling, condensate film in the region from the beginning of condensation until the occurring of merging waves shows instantaneous events, which cannot be captured by the experiments, like the low-frequency fluctuation of the laminar region with ripple waves and the evolution of surface instability into big surface waves. It allows to see further the details of the influence of the wave on the substrate up to the wall, where the pressure and the absolute wall vorticity are relatively strongly increased beyond the wave crest. By comparing to the theoretical and experimental results of the falling film without condensation, the similarities and the difference in film thickness as well as wavelength, celerity and frequency is pointed out.

REFERENCES

1. E. Marschall and C. Y. Lee, Stability of condensate flow down a vertical wall, *Int. J. Heat Mass Transfer* **16,** 41–48 (1973).
2. A. E. Dukler and O. P. Bergelin, Characteristics of flow in falling liquid films, *Chem. Engng Progr.* **48,** 557–563 (1952).
3. R. P. Salazar and E. Marschall, Three dimensional surface characteristics of a falling liquid film, *Int. J. Multiphase Flow* **4,** 487–496 (1978).
4. W. Nusselt, Die Oberflaechenkondensateion des Wasserdampfes, *VDI Zeitschrift* **60,** 541–546; 569–575 (1916).
5. W. M. Rohsenow, Heat transfer and temperature distribution in laminar falling film, *Trans. ASME* **78,** 1645–1648 (1956).
6. U. Grigull, Waermeuebertragung bei der Kondensation mit turbulenter Wasserhaut, *Forsch. Ing.-Wesen* **13,** 49–57 (1942).
7. A. M. Binnie, Experiments on the onset of wave formation on a film of water flowing down a vertical plate, *J. Fluid Mech.* **2,** 551–553 (1957).
8. P. L. Kapitza and S. P. Kapitza, Wavy flow of thin layers of viscous fluid, *Collected papers of P. L. Kapitza* Vol. 2, pp. 662–709. Pergamon Press, New York (1965).
9. F. P. Stainthorp and S. M. Allen, The development of ripples on the surface of a liquid film flowing inside a vertical tube, *Trans. Inst. Chem. Engrs* **443,** T85–T91 (1965).
10. L. O. Jones and S. Whitaker, An experimental study of falling liquid films, *A.I.Ch.E. Jl* **12,** 787–804 (1966).
11. K. J. Chu and A. E. Dukler, Statistical characteristics of thin wavy films, Part II, Studies of the substrate and its wave structure, *A.I.Ch.E. Jl* **20,** 695–706 (1975).
12. K. J. Chu and A. E. Dukler, Statistical characteristics of thin wavy films, Part III, Structure of the large waves and their resistance gas flow, *A.I.Ch.E. Jl* **21,** 583–593 (1975).
13. T. D. Karapantsios, S. V. Paras and A. J. Karabelas, Statistical characteristics of free falling films at high Reynolds numbers, *Int. J. Multiphase Flow* **14,** 1–21 (1989).
14. V. Penev, V. S. Krylov, C. H. Boyadjiev and V. P. Vorotilin, Wavy flow of thin liquid films, *Int. J. Heat Mass Transfer* **15,** 1395–1406 (1972).
15. R. I. Hirshburg and L. W. Florschuetz, Laminar wavy-film flow: Part I, Hydrodynamic analysis, *Trans. ASME J. Heat Transfer* **104,** 452–458 (1982).
16. R. I. Hirshburg and L. W. Florschuetz, Laminar wavy-film flow: Part II, Condensation and evaporation, *Trans. ASME J. Heat Transfer* **104,** 459–464 (1982).
17. V. D. Rao and P. K. Sarma, Condensation heat transfer on laminar falling film, *Trans. ASME J. Heat Transfer* **106,** 518–523 (1984).
18. N. Brauner, Modelling of wavy flow in turbulent free falling films, *Int. J. Multiphase Flow* **15,** 505–520 (1989).
19. B. Bach and J. Villadsen, Simulation of the vertical flow of a thin wavy film using finite-element method, *Int. J. Heat Mass Transfer* **27,** 815–827 (1984).
20. F. K. Wasden and A. E. Dukler, Numerical investigation of large wave interaction on free falling film, *Int. J. Multiphase Flow* **15,** 357–370 (1989).
21. D. M. Moalem, N. Brauner and G. F. Hewitt, Flow patterns in wavy thin films: numerical simulation, *Int. Commun. Heat Mass Transfer* **16,** 655–666 (1989).
22. J. C. Y. Koh, E. M. Sparrow and J. P. Hartnett, Two phase boundary layer in laminar condensation, *Int. J. Heat Mass Transfer* **2,** 69–82 (1961).
23. T. Ueda and H. Tanaka, Measurement of velocity, temperature and velocity fluctuation distribution in falling liquid films, *Int. J. Multiphase Flow* **15,** 261–272 (1975).
24. W. M. Rohsenow and J. P. Hartnett (eds), *Handbook of Heat Transfer*, Chap. 12-9. McGraw-Hill, New York (1973).
25. W. J. Minkowycz and E. M. Sparrow, Condensation heat transfer in the presence of non-condensables, interface resistance, superheating, variable properties and diffusion, *Int. J. Heat Mass Transfer* **9,** 1677–1682 (1966).
26. T. Kawamura and K. Kuwahara, Computation of high Reynolds number flow around a circular cylinder with surface roughness, A.I.A.A. Paper No. 84-0340, 1–11 (1984).
27. T. Miyauchi and M. Tani, Numerical analysis of homogeneous and isotropic turbulence by using third order upwind finite-difference method (in Japanese), *Trans. JSME* **B53**(486), 388–392 (1987).
28. G. Comte-Bellot and S. Corrsin, Simple Eulerian line correlation of full narrow band velocity signals in grid-generated 'isotropic' turbulence, *J. Fluid Mech.* **48,** 273–337 (1971).
29. E. Stuhlträger, T. Miyauchi and F. Hussain, Coherent structures in excited laminar and turbulent jets: comparison of direct numerical simulation with laboratory experiments, *Proc. 4th Asian Congress of Fluid Mechanics*, Vol. 2, pp. A105–A108 (1989).
30. R. A. Gentry, R. E. Martin and B. J. Daly, An Eulerian difference method for unsteady compressible flow problems, *J. Computational Physics* **1,** 87–118 (1966).
31. M. A. Shapiro and J. J. O'Brien, Boundary conditions for fine-mesh limited-area forecasts, *J. Appl. Meteorology* **9,** 345–349 (1970).
32. R. P. Salazar and E. Marschall, Time-average local thickness measurement in falling liquid film flow, *Int. J. Multiphase Flow* **4,** 405–421 (1978).
33. S. Portalski, Studies of falling liquid film flow, *Chem. Engng Sci.* **18,** 787–804 (1963).
34. G. D. Fulford, Gas–liquid flow in an inclined channel, Ph.D. dissertation, University of Birmingham, U.K. (1962).
35. D. A. Charvonia, An experimental investigation of the mean liquid film thickness and the characteristics of the interfacial surface in annular two-phase flow, ASME Paper, No. 61-WA-243 (1961).
36. S. R. Tailby and S. Portalski, Hydrodynamics of liquid films flowing on a vertical surface, *Trans. Inst. Chem. Engrs* **38,** 324–330 (1960).
37. F. W. Pierson and S. Whitaker, Some theoretical and experimental observations of the wave structure of the falling liquid film, *Ind. Engng Chem. Fundam.* **16,** 401–408 (1977).
38. F. P. Stainthorp and R. S. Batt, The effect of co-current and counter-current air flow on the wave properties of falling liquid film, *Trans. Inst. Chem. Engrs* **45,** T372–T382 (1967).